RSC Applied Interfaces

ROYAL SOCIETY OF CHEMISTRY

PAPER

View Article Online
View Journal | View Issue

Check for updates

Cite this: *RSC Appl. Interfaces*, 2025, **2**, 1288

A purposefully engineered bimetallic graphene oxide nanosphere composite for visible light-driven eradication of organic fluorescent dyes†

Krishan Kumar

Received 9th June 2025,
Accepted 3rd July 2025

DOI: 10.1039/d5lf00166h

rsc.li/RSCApplInter

Water pollution of natural water sources has been rapidly augmented because of the continuous discharge of wastewater as a result of industrial globalization. However, conventional tools and technologies for wastewater treatment are insufficient to remediate the pollutants. Thus, we devised a simple and efficient neodymium-doped zinc sulfide (ZnS)-anchored graphene oxide (GO) nanosphere (Nd@ZnS:GO-NS) composite *via* co-precipitation and sonochemical techniques. Nd@ZnS:GO-NSs were tailored *via* surface charge-induced strained wrapping phenomenon by rolling up of annealed GO nanosheets, and the diameters were mostly in the range of 50–200 nm. These Nd@ZnS:GO-NSs were employed for the photodegradation of the cationic organic dyes (CODs) methyl orange (MO) and Coomassie brilliant blue red (BBR). Complete (100%) photodegradation of MO and BBR was observed with Nd@ZnS (3.50 h and 3.00 h, respectively) and Nd@ZnS:GO-NSs (180 min and 80 min, respectively). Optimized conditions of pH = 8, COD dosage = 20 mgL^{-1}, and Nd@ZnS:GO-NS dosage = 20 mg showed excellent degradation activities. Although both Nd@ZnS and Nd@ZnS:GO-NSs served as photocatalysts, among them, Nd@ZnS:GO-NSs showed excellent photosensor activities owing to their fast charge mobility, superior electronic conductivity, and improved surface activity, supplementing the role of 2D-GO in multicyclic reusability. Moreover, the negative (e^-) hole pairs generated from Nd@ZnS:GO-NSs interfaced for a longer time with MO dye (with a stronger azo (–N═N–) group and one SO_3^- group) than with BBR dye (with two SO_3^- groups and a quaternary nitrogen (═N^+–) group). Nd@ZnS:GO-NSs may open up new opportunities for the rational construction of effective photocatalysts for fundamental research and other applications. This strategic bifurcation of nanomaterials can be extended to doping with other nanomaterials, thereby advancing the development of nanostructures to the next level.

1. Introduction

Water pollution has emerged as a critical global issue in recent decades, significantly threatening both environmental sustainability and public health.[1] The prominent reason for water pollution is the discharge of huge amounts of wastewater directly into the freshwater bodies as a result of industrial, agricultural, and domestic activities.[2] In particular, effluents from chemical industries, along with expired and unregulated materials, substantially contribute to aquatic pollution.[3] A major concern within this context is the widespread use of synthetic cationic organic dyes (CODs), such as azo-based methyl orange and Coomassie brilliant blue.[4,5] These dyes are persistent, non-biodegradable, and toxic, posing serious ecological risks and health hazards,[6] including skin and eye irritation, respiratory problems,[7] and even carcinogenic effects.[8] Furthermore, their accumulation disrupts aquatic ecosystems, reduces biodiversity, and compromises soil quality through trophic-level contamination.[9]

CODs are extensively utilized in a broad range of fields, including textiles, printing, leather processing, plastics, polymers, medical diagnostics, protein/DNA labelling, laser technology, optical sensing, and security authentication.[10,11] Their widespread use is largely attributed to their structural stability, particularly because of the presence of complex aromatic (*e.g.*, naphthalene) rings, which also makes their removal from wastewater challenging.[12,13] Conventional treatment approaches—biological degradation, filtration, chlorination, and oxidative methods (*e.g.*, ozonation, Fenton, and photo-Fenton processes)—have demonstrated limited efficiency and may produce secondary pollutants (Table S2†).[14,15] Alternatively, photodegradation has gained significant attention owing to its high efficiency, minimal

School of chemical Sciences, Central University of Gujarat, Gandhinagar, Sector-30 (382030), India. E-mail: Krishan8053649040@gmail.com

† Electronic supplementary information (ESI) available: Plots of DLS, BET, SEM, AFM, TGA, P-XRD, HR-TEM, and tables of ICP-OES and comparative studies. See DOI: https://doi.org/10.1039/d5lf00166h

secondary waste generation, and adherence to sustainable treatment goals.[9] Recent research has focused on the design and fabrication of advanced nanostructured photocatalysts, particularly transition metal sulfides (TMSs) with tailored core/shell architectures, which offer enhanced biocompatibility, catalytic activity, conductivity, and multifunctionality across applications such as biosensing, drug delivery, and energy storage.[16,17]

However, the scarcity and high cost of TMS nanoparticles limit their large-scale application.[18] To overcome these limitations, surface engineering through lanthanide ion (Ln^{3+})-doping followed by GO coating has been explored. Doping with Ln^{3+} modulates the bandgap, suppresses the electron–hole recombination, and enhances the photocatalytic and optical properties. Concurrently, GO—rich in sp^2-hybridized carbon and oxygen-containing functional groups—improves dispersion, thermal stability, surface functionality, and photocatalytic efficiency owing to its high surface area and excellent electronic conductivity.[19] Crystalline TMS materials have been successfully applied in areas including solar energy conversion, microwave shielding, rechargeable batteries, and wastewater remediation. In particular, lanthanide-doped TMS photocatalysts have shown superior light absorption and catalytic performance in degrading water-soluble organic effluents.[20]

In this study, we synthesized Nd-doped ZnS nanospheres anchored on GO sheets (Nd@ZnS:GO-NSs) *via* a sonochemical-assisted co-precipitation method, followed by a surface charge-induced strained wrapping phenomenon. These engineered nanospheres demonstrated enhanced photocatalytic efficiency under solar irradiation for the degradation of hazardous cationic dyes—methyl orange and Coomassie brilliant blue—outperforming pristine GO in terms of thermal stability and reusability over six consecutive cycles. The improved photocatalytic activity was attributed to the synergistic effects of Nd doping, which improved charge separation and photosensitization, and GO matrix, which facilitated better electron transport and structural flexibility. Moreover, the high surface-area-to-volume ratio of the nanospheres enhanced the light absorption, exploiting the quantum size effects for superior photodegradation performance.[21] To date, no nanospheres of GO have been reported using a lanthanide dopant in ZnS lattices. Nd@ZnS:GO-NSs may open a new frontier for fundamental research and applications on effective photocatalysts for dye removal. These nanomaterials may be extended through doping with other metals and fabricating related nanostructures. Nd@ZnS:GO-NSs might be futuristic nanomaterials owing to their outstanding capability to mold the functional sites *via* surface charge, inducing a strained wrapping phenomenon.

2. Experimental section

2.1. Materials

Graphite flakes (Gt, <45 μm, ≥99.99%), concentrated sulfuric acid (H_2SO_4, 98%), hydrogen peroxide (H_2O_2, ≥85 wt% in H_2O), zinc chloride ($ZnCl_2$, ≥98.9%), neodymium chloride ($NdCl_3{\cdot}H_2O$, 99.9%), iron(II) sulfide (FeS, 99.9%), brilliant blue red (BBR, ≥98%), methyl orange (MO, ≥95%), and phenolphthalein (97%) were procured from Sigma-Aldrich. Potassium permanganate ($KMnO_4$, ≥98%), hydrochloric acid (HCl, 36%), and sodium hydroxide (NaOH, 99%) were obtained from Rankem; petroleum ether (boiling range 40–60 °C) from SRL; and absolute alcohol (99.9%) from Scvuksmandli Ltd., India.

2.2. Synthesis of ZnS and neodymium-doped ZnS (Nd@ZnS)

ZnS was synthesized *via* co-precipitation using 100 mg of $ZnCl_2$ and 0.0050 M NaOH in 100 mL of distilled water.[22] NaOH was added dropwise to the $ZnCl_2$ solution under constant stirring until white $Zn(OH)_2$ precipitated. The mixture was stirred at 400 rpm and maintained at 80 °C for 12 h.[23] The precipitate was washed with distilled water and diluted with HCl to remove the residual Cl^- and OH^- ions, followed by centrifugation at 8000 rpm for 15 min. H_2S gas was generated by reacting 1.00 g of FeS with 200 mL of dilute HCl in a Kipp's apparatus and bubbled through $Zn(OH)_2$ suspension for 10–15 min, forming ZnS.[24] The product was washed, centrifuged (8000 rpm, 20 min), and dried in a vacuum oven at 70 °C for 24 h. For bimetallic ZnS (Nd@ZnS), 50 mg of ZnS and 10 mg of $NdCl_3{\cdot}6H_2O$ were dissolved in 100 mL of distilled water, sonicated for 30 min, and stirred at 90 °C at 650 rpm for 6 h. The final product was washed and dried at 60 °C (Scheme S1†).

2.3. Synthesis of graphene oxide (GO)

GO was synthesized according to a previously reported procedure. Typically, Gt (5.00 g) and $KMnO_4$ (15.00 g) were used to prepare a 200 mL oxidizing mixture of $H_2SO_4 : H_3PO_4$ in a 15 : 6 ratio. The oxidizing mixture was poured dropwise into a round bottom (RB) flask and placed in an ice bath with continuous stirring (greenish appearance). The resultant mixture was stirred at 55 °C and 650 rpm for 12 h under an oil bath to avoid heat dissipation. After refluxing, it was maintained at room temperature for 4–5 h, and ice-cold water was cautiously added to it (dark red). Subsequently, 3 mL of H_2O_2 (30%) was added to the mixture with continuous stirring for 10 min, producing a mixture of graphite oxide (whitish brown).[25] The resultant mixture was washed with distilled water, dil. HCI, and ethanol, followed by centrifuging at 8000 rpm for 20 min (dark brown). The product was coagulated with petroleum ether and extracted in a Petri dish. The GO sheets were exfoliated, followed by sonication for 2–3 h at 28 kHz; a brownish suspension was obtained and was dried at 70 °C for 12 h (Scheme 1).

2.4. Synthesis of Nd@ZnS:GO-NSs *via* the sonochemical method

Initially, 150 mg of 2D-GO sheets were dispersed in 100 mL of water and delaminated using a sonochemical technique at 28 kHz and 90 °C for 3 hours, resulting in a stable colloidal suspension.[27] The solution of GO nanosheets and 100 mg of

Nd@ZnS was homogenized in 200 mL of distilled water and treated further *via* ultrasonication at 28 kHz and 90 °C for 3 hours, resulting in a homogeneous suspension (dark brown). The resultant mixture was washed with distilled water, dil. HCl, and ethanol (4–5 times), followed by centrifugation at 8000 rpm for 10 min. $AgNO_3$ and phenolphthalein tests ensured the complete removal of Cl^- and OH^- ions. The resultant composite with a bright brownish appearance was dried in a vacuum oven at 70 °C for 12 h (Scheme S2†).

3. Results and discussions

The synthesized nanomaterial was initially analyzed using Fourier transform infrared spectroscopy (FTIR). The stretching vibrations at 1071, 1400, 1250, 1750, and 1626 cm^{-1} were ascribed to –O–, –CHO, ═CO, –COOH, and –OH oxygenated moieties,[28] while a broader peak at 3351 cm^{-1} for –OH was observed for 2D-GO nanosheets (Fig. S1a†). The IR peaks of Nd@ZnS:GO-NSs at 678, 958, 1405, and 1634 cm^{-1}, along with the functional moieties of GO sheets, indicated a favourable wrapping of the GO nanosheets on Nd@ZnS nanoparticles.[29] A broad –OH peak at 3400–3440 cm^{-1} indicated that a fraction of the C atoms existed on the surface was hydroxylated, which offered Nd@ZnS:GO-NSs with good dispersion in water (Fig. 1a). The crystallinity and diffracted planes of the as-synthesized nanomaterials were detected using XRD, and the GO nanosheet inferred the crystallinity of (001) diffracted planes at 2θ = 9.82° (Fig. S1b†). Moreover, the patterns of Nd@ZnS and Nd@ZnS:GO-NSs indicated three major peaks in addition to a broader peak corresponding to the (111), (220), (311), and (331) planes, respectively (JCPD card no. 77-21000). The Nd@ZnS nanomaterial was uniformly distributed on the surfaces of the GO nanosheets, confirming the successful synthesis of Nd@ZnS:GO-NSs.[30] The Nd dopant and GO nanosheets did not affect the ZnS crystallinity but rather sharpened the intensity and broadened the *d*-spacing within the same XRD peaks and corresponding planes (Fig. 1b). The surfaces of Nd@ZnS:GO-NSs were smoothened with −18.74 mV surface charge compared with GO and Nd@ZnS with surface charges of −29.81 mV and +25.84, respectively (Fig. 1c). Nd@ZnS with a positive surface charge strongly engaged with the outer surface of the GO nanosheet *via* coulombic interactions, fabricating negatively charged Nd@ZnS:GO-NSs (Fig. S1c†). Thus, Nd@ZnS nanomaterials were surface-modified with a positive surface charge and compensated with the negative surface charges of GO nanosheets.

The porosity of GO and Nd@ZnS:GO-NSs was analyzed with N_2 adsorption–desorption at 77 K; the average surface area, pore diameter, and pore volume were 25.893 $m^2\ g^{-1}$, 24.590 nm, and 0.0089 cc g^{-1}, respectively, while the values of 182.219 $m^2\ g^{-1}$, 5.438 nm, and 0.243 cc g^{-1} were calculated from non-local density functional theory (NLDFT) (Fig. 1d and e). The Nd@ZnS:GO-NSs isotherm data fitted well with a type II isotherm according to the IUPAC owing to the presence of macropores and nanospheres and a smaller diameter compared with that of 2D-GO sheets. The larger surface area of Nd@ZnS:GO-NSs with interstitial cavities indicated a higher N_2 adsorption–desorption and improved structural stability upon doping and coating the ZnS lattice (Fig. S1d†). The morphology and structure of ZnS, Nd@ZnS, GO, and Nd@ZnS:GO-NSs were characterized using HR-TEM and AFM analyses (Fig. 2). A 0.5 mg/50 mL solution of Nd@ZnS:GO-NSs was prepared to investigate the

Scheme 1 Preparation of graphene oxide: (a) mixture of Gt and $KMnO_4$, (b) dropwise addition of oxidizing mixture (H_2SO_4 : H_3PO_4), and (c) stirring at 55 °C at 650 rpm. (d) Mixture after 12 hours and (e) at room temperature, (f) addition of ice-cold water at a slow rate, (g) treatment with H_2O_2 (30%), (h) coagulation with petroleum ether (i) corresponding image after 2 hour, and (j) developed 2D-GO sheet by using the modified hummer's method.[26]

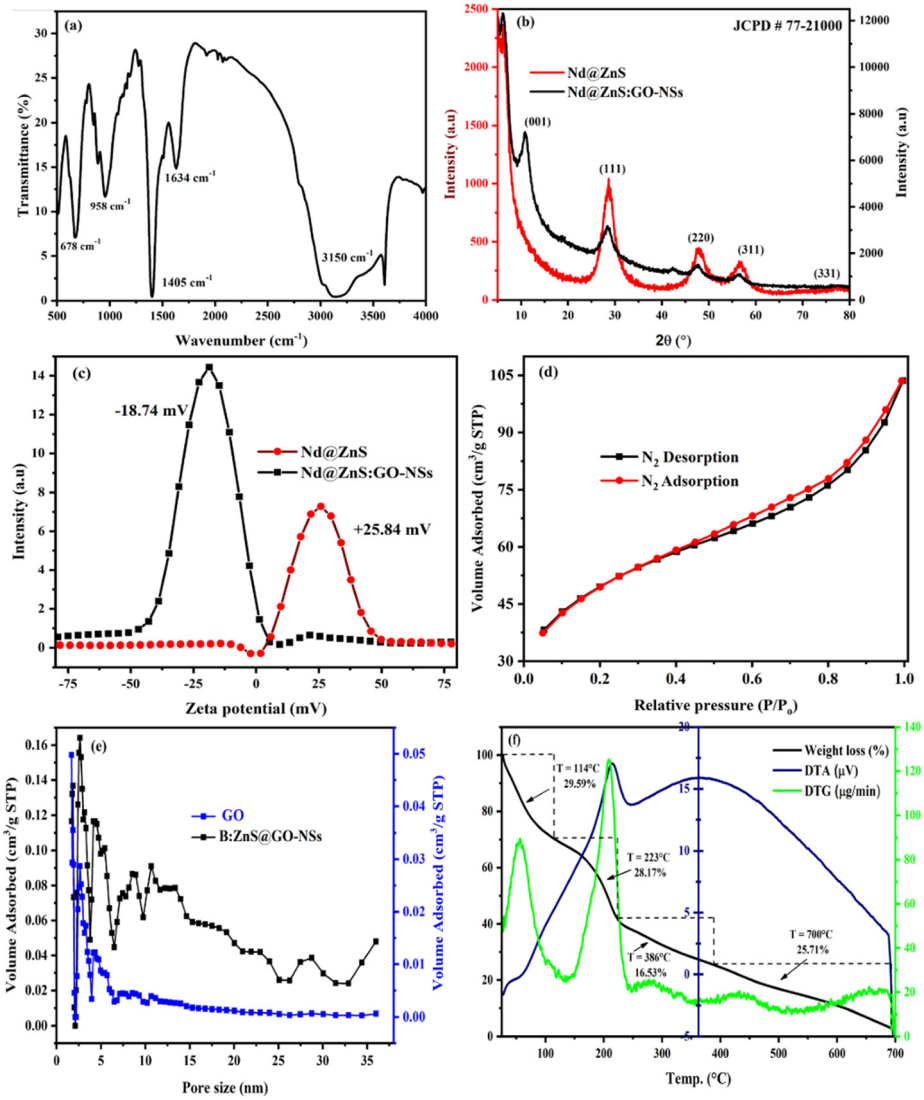

Fig. 1 (a) FT-IR spectrum of Nd@ZnS:GO-NSs, (b) P-XRD pattern of Nd@ZnS:GO-NSs (black) and Nd@ZnS (red), (c) comparative zeta potential of Nd@ZnS:GO-NSs (black) and Nd@ZnS (red), (d) N_2 adsorption–desorption isotherm of Nd@ZnS:GO-NSs at 77 K, (e) comparative pore size of GO (blue) and Nd@ZnS:GO-NSs (black), and (f) TGA, DTA, and DTG analysis of Nd@ZnS:GO-NSs.

morphology. To be imaged, Nd@ZnS:GO-NSs were placed in a vacuum for direct exposure of fast-moving electrons.[31] Nd@ZnS:GO-NSs did not break or vibrate during the observation, which suggested there were no adhered water molecules or other impurities on Nd@ZnS:GO-NSs. Micrographs of the collapsed nanospheres showed a strong encapsulation of Nd@ZnS nanomaterials (Fig. 2c). Initially, the ZnS lattice included suppressed nanoparticles, and upon doping with Nd, the spherical morphology was converted to a crystalline structure (Fig. S2†). Nd@ZnS upon wrapping with GO nanosheets resulted in a nanospherical shape with a diameter of 50–200 nm. The coulombic and electrostatic interactions between the unlike surface charges of Nd@ZnS and GO nanosheets were optimized such that the GO nanosheets molded into a spherical shape, followed by a surface charge-induced strained wrapping phenomenon (Scheme 2). The high-resolution HR-TEM images of Nd@ZnS:GO-NSs shown in Fig. 2a–d indicated that the nanosheets were well-doped with ordered layers of carbon atoms.[32] Nd@ZnS:GO-NSs were found to be aggregated, indicating a high yield of the nanospheres. The diameters of the 60–80% of the Nd@ZnS:GO-NSs lied in the range of 50–200 nm.

The variation in diameters was attributed to the different areas of the nanosheets in the pristine GO. AFM analysis was conducted using a silica wafer in non-contact mode to capture the unique morphology and thickness of the as-synthesized nanocomposites. The AFM micrographs indicated an overlapping of nanospheres compared with pristine nanomaterials. Uniform size distribution of Nd@ZnS:GO-NSs was illustrated in AFM images, which was consistent with the

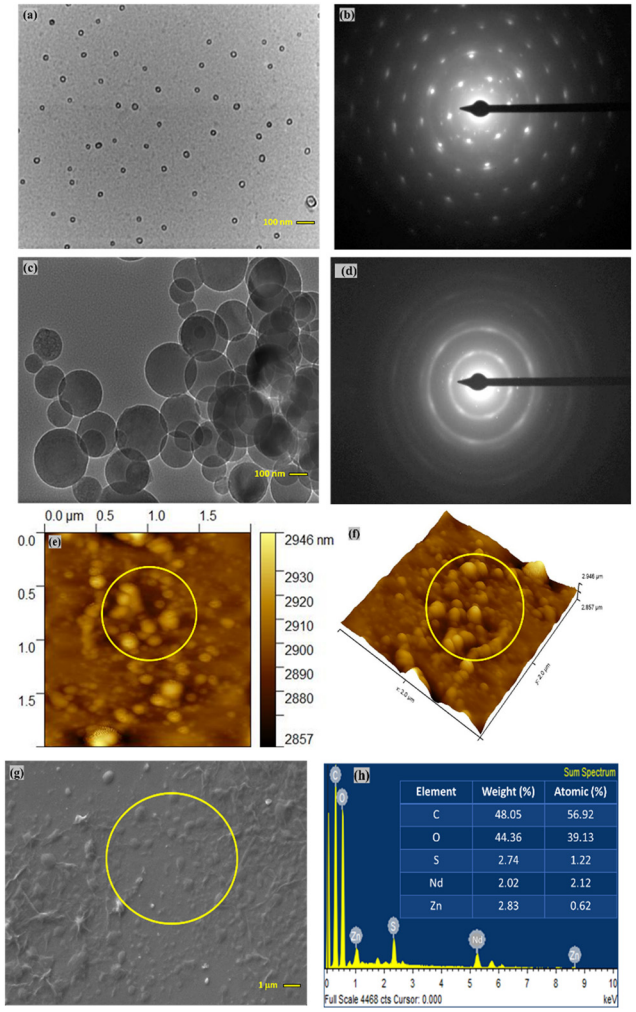

Fig. 2 (a–d) HR-TEM images with SAED pattern for Nd@ZnS and Nd@ZnS:GO-NSs. (e and f) AFM micrographs of Nd@ZnS:GO-NSs with a 3D view. (g and h) SEM image with EDS of Nd@ZnS:GO-NSs.

TEM images (Fig. 2e and f). The elemental compositions of the as-synthesized nanomaterials confirmed the effective doping and coating of Nd and GO with the ZnS lattice (Table S1†). Thermogram of Nd@ZnS:GO-NSs indicated weight losses of 29.59%, 28.17%, 16.53%, and 25.71% at 114, 223, 386, and 700 °C, respectively, compared with the 32.06, 32.41, and 35.53% at 104, 207, and 700 °C with 2D-GO nanosheets. The weight loss transition from 104–114 °C inferred absorbed moisture, while the other weight losses indicated a core lattice disruption. Thus, Nd@ZnS:GO-NSs were confirmed to possess better heat absorption capacity than the 2D-GO nanosheet owing to their enhanced thermal conductivity (Fig. 1f and S1g†).

3.1. Formation of GO nanospheres

The morphological formulation of nanospheres was in-depth investigated using various analytical techniques and rationalized *via* surface charge-induced-strained wrapping phenomena. 2D-GO nanosheets were transformed into nanospheres after amalgamating them with neodymium-doped ZnS nanoparticles.[33] This transformation was driven by Coulombic interactions, where the negatively charged and polarized surface functional sites of the GO nanosheets were preferably oriented towards high-density Lewis acidic sites of positively charged Nd@ZnS to minimize the combined surface charge and surface energy.[34] However, upon wrapping the Nd@ZnS nanoparticles, the strong electrostatic interactions led to a significant change in the spatial morphology, as shown in Fig. 2. This study is the first successful synthesis of GO nanospheres, offering a novel morphological adaptation with enhanced photosensing functionality. These nanospheres were subsequently employed in photodegradation experiments targeting MO and Coomassie BBR, which are two major organic pollutants in industrial effluents. The GO nanospheres exhibited high photodegradation efficiency owing to their increased surface area, improved charge separation, and the structure-function synergism between GO and Nd@ZnS. This innovative approach highlighted the potential of surface charge-induced morphological changes in materials for improved environmental remediation

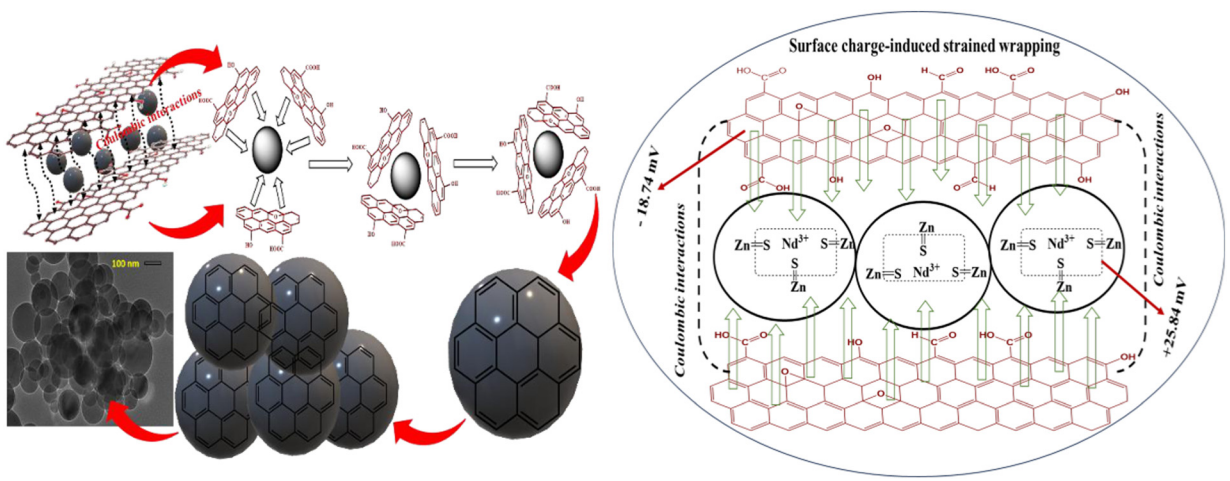

Scheme 2 Formation of Nd@ZnS:GO nanospheres *via* a surface charge-induced strained wrapping phenomenon.

applications, specifically in the degradation of persistent organic pollutants.[13]

3.2. Photodegradation activities of Nd@ZnS and Nd@ZnS:GO-NSs

After the successful synthesis of GO nanospheres, the photodegradation activities of the as-prepared Nd@ZnS and Nd@ZnS:GO-NSs were evaluated based on their performance in degrading cationic organic dyes (CODs) from wastewater solutions (Fig. 3). The parameters for the dye degradation efficiency, including the amount of photocatalyst, contact time, and pH of the solution were studied and optimized. The reusability and kinetics of the reaction were investigated and discussed in detail. The amount of dyes photodegraded by Nd@ZnS:GO-NSs was noted as the degradation efficiency or removal capacity and was calculated using the following equation:

$$\text{Degradation efficiency } (\%) = \frac{C_0 - C_t}{C_0} \times 100 \qquad (1.0)$$

The kinetics of COD photodegradation in the presence of

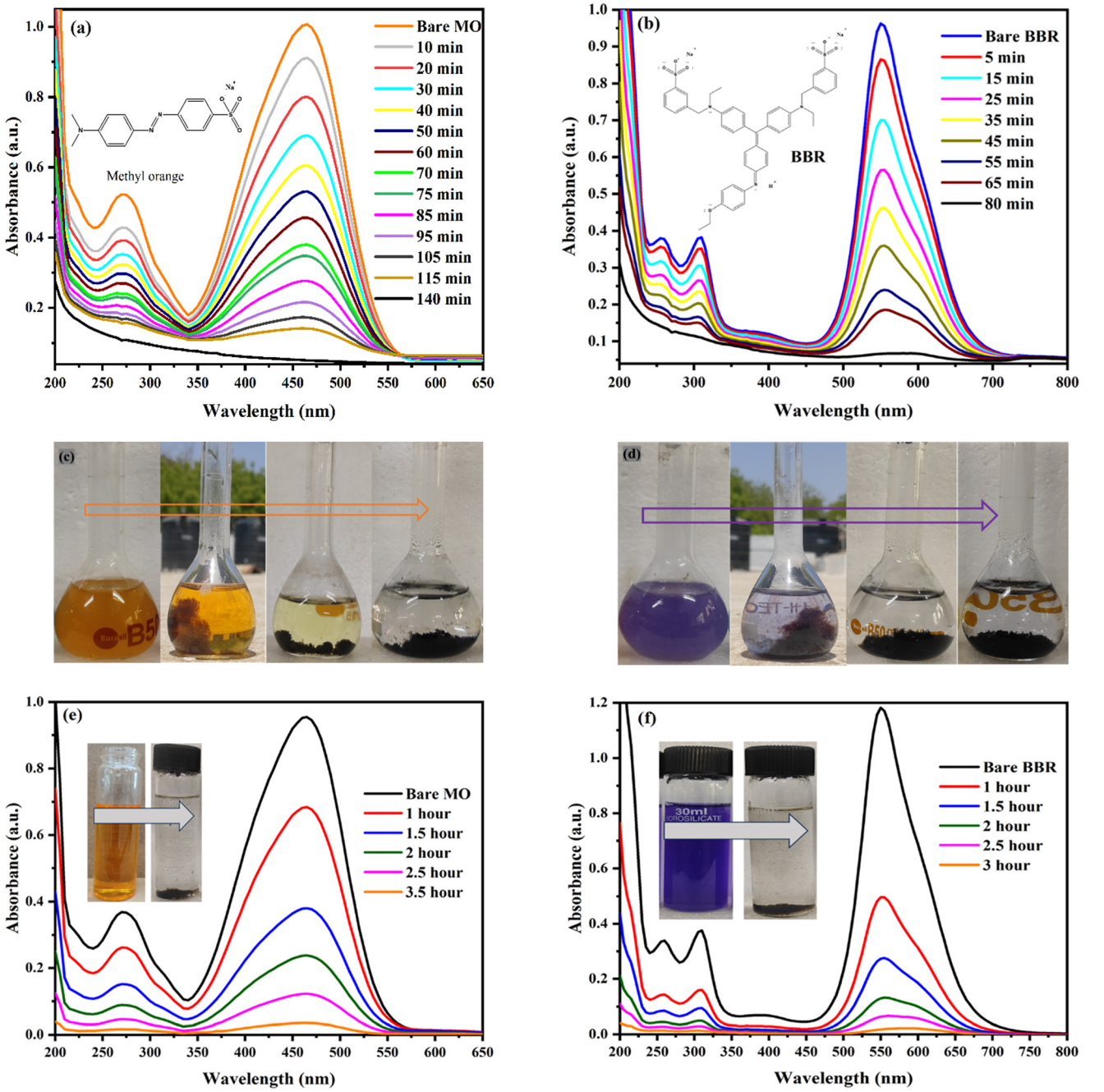

Fig. 3 Photodegradation activities using catalysts (a–d) Nd@ZnS:GO-NSs and (e and f) Nd@ZnS for MO and BBR dyes, respectively, under sunlight.

Nd@ZnS:GO-NSs under sunlight was studied, and it was found that they followed the Langmuir–Hinshelwood model, indicating first-order kinetics. The kinetic study was executed using 20 mg L^{-1} of COD and 20 mg of Nd@ZnS:GO-NSs. The Langmuir–Hinshelwood kinetic model is given by the following equation:

$$\ln(C_0/C_t) = kt \quad (1.1)$$

where k is the rate constant of the photodegradation reaction, C_0 and C_t are the concentrations at the initial and 't' time of the COD molecule in the reaction mixture, respectively. The value of k was calculated from the straight line obtained by plotting $\ln(C_0/C_t)$ against t (eqn (1.1)). The quantum yields for the CODs were calculated following a previous study. The absorbance of UV-visible band spectra was used to calculate the quantum yield using Einstein's eqn (1.2):

$$E = mc^2, \quad (1.2)$$

$$\text{abs} = \varepsilon lc,\ \Delta c = \frac{\Delta\text{Abs}}{\varepsilon l} \quad (1.3)$$

where m is the mass derived from eqn (1.2), Δc is the change in concentration, ΔAbs is the change in absorbance, and c is the speed of a light/photon (3×10^8 m s^{-1}).

3.3. Effect of pH

The pH experiment of the solution played a crucial role in determining the efficiency of photodegradation, as pH was a more decisive parameter that affected the surface charge properties and size and clustering of Nd@ZnS:GO-NSs.[18] Therefore, the photodegradation efficiency directly depended on the pH of the solution. The surface charge of Nd@ZnS:GO-NSs (−18.74 mV) directly influences the

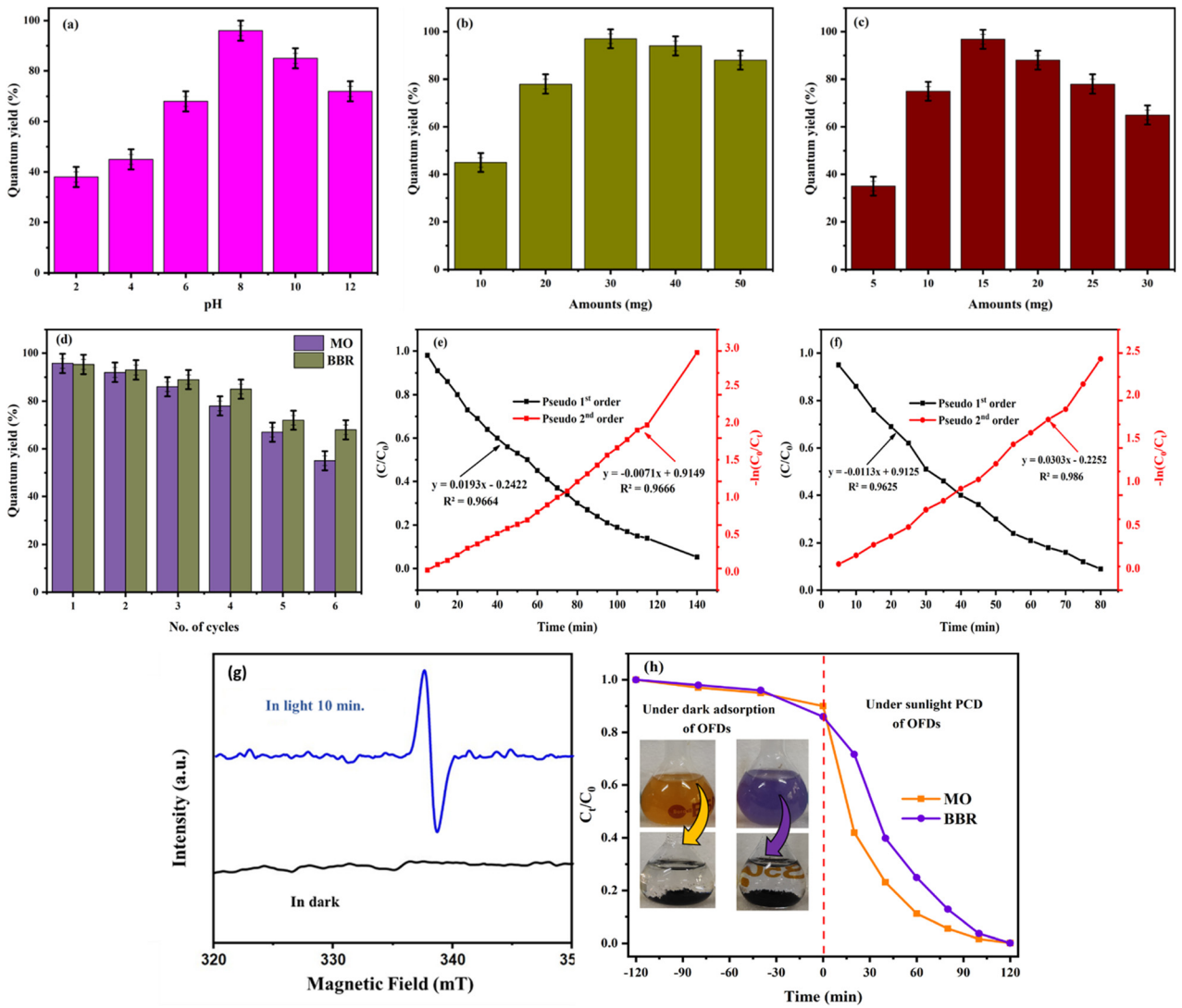

Fig. 4 (a) Effect of pH on photodegradation activities. (b and c) Effect of Nd@ZnS:GO-NSs dosage on MO and BBR photodegradation. (d) Reusability of the catalyst. (e and f) Kinetics of the catalyst. (g) EPR analysis of the catalyst. (h) Degradation kinetics in the dark and in the presence of sunlight.

degradation process, particularly in relation to pH optimization. The effect of pH on degradation efficiency (%) was studied by varying the pH from 2–12 in the presence of Nd@ZnS:GO-NSs (25 mg each) and 20 mg L^{-1} of MO and BBR dye solutions. The pH adjustment experiment was conducted using aqueous solutions of 0.1 M HCl and NaOH. CODs and Nd@ZnS:GO-NSs were placed under sunlight for 4 h. The degradation efficiency (%) was determined as per eqn (1.0) and based on the gradual decline in the absorbance intensity of the COD solution with respect to their maximum wavelength (Fig. 3). The maximum COD degradation using Nd@ZnS:GO-NSs was detected at pH 8 and 9. The maximum degradation efficiency was observed at these specific pH values, which can be attributed to the gradual increment in the concentration of OH^- ions.[35] The hydroxyl radicals are considered as oxidising agents for photodegradation; thus, the maximum degradation of dyes can be achieved under alkaline solution conditions (Fig. 4a). The maximum photodegradation of MO and Coomassie BBR was in the range of 98–99.02% efficiency within 80–140 min, which ranked the best among the previously reported values (Table S2†). The electrostatic and coulombic attractions between the COD species and Nd@ZnS:GO-NSs (−18.74 mV) led to an enhanced dye adsorption rate on the surface of Nd@ZnS:GO-NSs. Thus, in an alkaline solution, the competition of OH^- ions for getting adsorbed on the surfaces of Nd@ZnS:GO-NSs may limit the degradation efficiency. Moreover, under acidic conditions, the formation of H^+ ions promotes their attraction to the surface of Nd@ZnS:GO-NSs *via* coulombic forces, thereby influencing the degradation process (Fig. 4a).

3.4. Effects of dye dosage and contact time

The effects of COD concentration and irradiation time on the photodegradation of CODs using Nd@ZnS:GO-NSs were investigated at the optimized pH.[18] Initially, a 100 mL solution with a COD concentration range of 20–100 ppm was used for photodegradation over varying contact times of up to 4 hours under optimized conditions. Experiments were conducted using 25 mg of Nd@ZnS:GO-NSs mixed in COD solutions at pH 8. A gradual decrease in the intensities of UV-visible absorbance for MO and BBR at 460 nm and 550 nm wavelengths, respectively, was observed (Fig. 3a and b). After optimizing the photodegradation performance of Nd@ZnS, 97–98% degradation was observed in 3.5 (MO) and 3 hours (BBR) under sunlight. The maximum degradations were detected as 98.70% and 99.20% at 140 (MO) and 80 min (BBR) contact time using Nd@ZnS:GO-NSs, respectively (Fig. S3c and d†). On increasing the COD concentrations, the degradation efficiencies of Nd@ZnS and Nd@ZnS:GO-NSs decreased continuously. This may be due to the higher concentration of CODs hindering the photon transmittance, indicating the least photoactivation of Nd@ZnS and Nd@ZnS:GO-NSs, which affected the degradation efficiency. In addition, low production of hydroxyl radicals at higher COD concentrations hindered the photodegradation.[35]

3.5. Effect of the dosage of Nd@ZnS:GO-NSs

To investigate the effect of photocatalyst dosage on COD degradation efficiency, experiments were conducted under optimized conditions using 10–50 mg and 5–30 mg of Nd@ZnS:GO-NSs with MO and BBR, respectively. It was observed that the COD removal performance of Nd@ZnS:GO-NSs was enhanced with increasing the dosage. Nevertheless, the photodegradation efficiency decreased at higher Nd@ZnS:GO-NS dosages, which can be attributed to the coagulation of nanocomposites. This led to a reduction in the negative (e^-) and positive (h^+) hole numbers.[36] Thus, the penetration of the exposed photons through the solution was hindered by the overdosage of photocatalysts.[11] Accordingly, the electron–hole recombination rate was disrupted, leading to a decrease in the degradation efficiency (Fig. 4b and c).

3.6. Reusability of Nd@ZnS:GO-NSs

The reusability of the photocatalyst was examined through several experiments. 100 mL of COD solutions (20 ppm) were prepared and irradiated for 140 min (MO) and 80 min (BBR) using Nd@ZnS:GO-NSs as photocatalysts under optimized conditions. After subsequent cycles, the COD concentration was adjusted to 20 ppm, and the next photodegradation cycle was conducted. Nd@ZnS:GO-NSs performed desirably until the 6th cycle, offering efficient degradation. After that, the degradation efficiency gradually decreased up to the 6th cycle. This may be due to that, after the 6th cycle the functional sites of the photocatalysts were occupied to resist the hole-generating tendency, leading to a gradual decrease in the degradation efficiency (Fig. 4d). Thus, the optimized parameters for photodegradation were pH = 8, effluent dosage = 20 ppm, and catalyst dosage = 20 mg for excellent degradation activities. Thus, the as-synthesised Nd@ZnS and Nd@ZnS:GO-NSs acted as photocatalysts, and among them, Nd@ZnS:GO-NSs showed excellent photosensor activities, supplementing the role of GO nanosheet with 6 times reusability. Besides, MO required a longer time to photodegrade than BBR, which could be attributed to the stronger azo and sulphonic groups.[37] The hole pairs generated from Nd@ZnS:GO-NSs interfaced for a longer time with MO dye (with the stronger azo (–N═N–) and oneSO_3^- groups) than BBR (with two SO_3^- and a quaternary nitrogen (═N^+–) groups) (Fig. S3a and b†). The regenerated nanosphere-based adsorbents retained their structural and chemical integrities, as confirmed by multiple analytical techniques, including FT-IR, HR-TEM, and DLS. The FT-IR spectra indicated the presence of characteristic stretching frequencies, suggesting that the functional groups responsible for adsorption remained intact post-regeneration (Fig. S4†). HR-TEM images further corroborated these findings by revealing that the morphological features of the nanospheres were maintained without any noticeable collapse or degradation (Fig. 5a). The surface charge of the nanoparticles, as

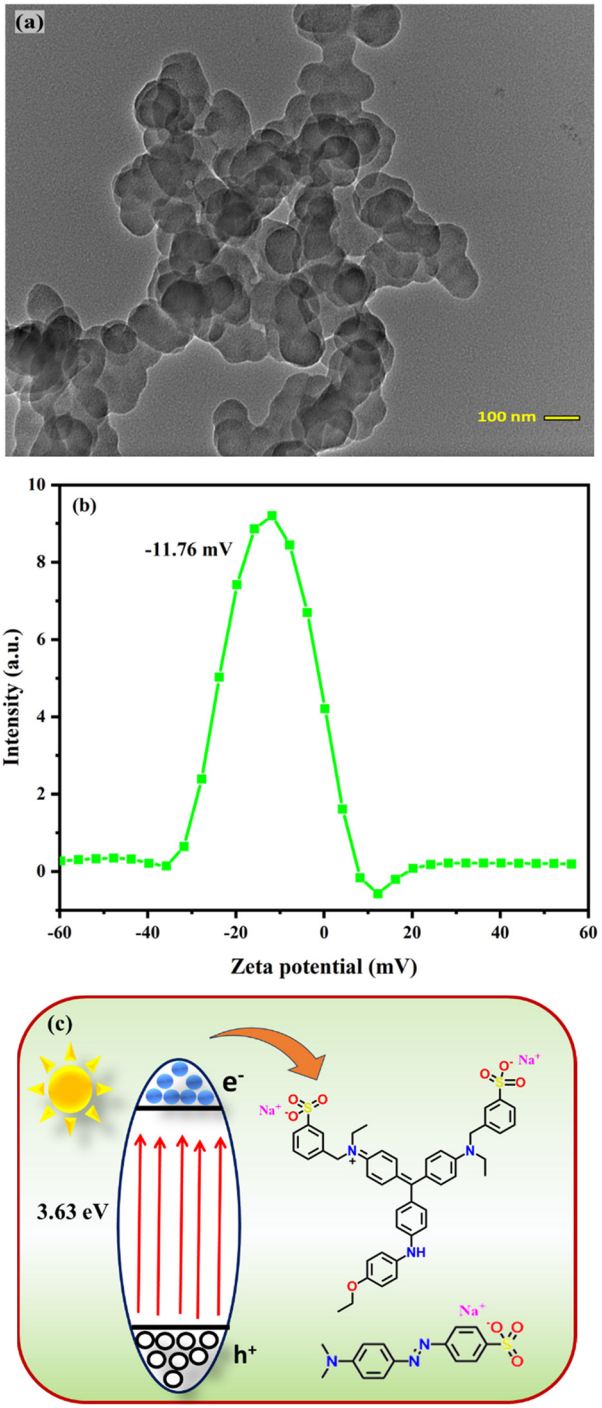

Fig. 5 Post metric analysis of Nd@ZnS:GO-NSs after regeneration: (a) HR-TEM image, (b) zeta potential and (c) plausible mechanism for the photodegradation of MO and BBR dyes under sunlight using Nd@ZnS: GO-NSs.

assessed using DLS, exhibited a notable decrease following dye degradation compared with their pristine counterparts. This reduction in zeta potential suggested alterations in the surface chemistry of the nanoparticles, potentially owing to the adsorption of dye molecules or the formation of degradation byproducts that modified the surface functional groups. Such changes can influence the electrostatic interactions between nanospheres and pollutants, thereby affecting the efficiency of the photodegradation processes (Fig. 5b). For instance, studies have shown that the surface charge of photocatalysts plays a crucial role in dye degradation efficiency, with variations in pH and surface modifications leading to significant differences in performance. Collectively, these analyses demonstrated that Nd@ZnS:GO-NS composites serve as robust and reusable platforms for the effective degradation of CODs in aqueous environments. The preservation of stability and resilience of these nanomaterials through multiple regeneration cycles underscore their potential for sustainable water purification applications.[38]

3.7. Plausible mechanism for photodegradation using Nd@ZnS:GO-NSs

In this study, the photodegradation of COD molecules was facilitated through a synergistic mechanism involving surface adsorption/desorption processes and efficient charge carrier dynamics in Nd-doped ZnS nanostructures integrated with GO (Nd@ZnS:GO-NSs). The GO nanosheets facilitated the transfer of photogenerated hole pairs at the Nd@ZnS interface and resisted the recombination of the hole pairs. The photoactivity of the bimetallic nanospheres was first confirmed using the EPR spectroscopy. Fig. 4g shows an intense signal after the exposure to visible light for 10 min. No signal was observed under dark conditions, which supported the electron–hole pair generation under visible light irradiation. Initially, dye molecules interacted with the catalyst surface *via* non-covalent interactions such as hydrogen bonding and π–π stacking. These interactions were enabled by the abundant oxygen-containing and π-conjugated functional groups present on the surface of GO and ZnS, which enhanced the adsorption of dye molecules. Upon visible light irradiation, the semiconductor component (ZnS) absorbed photons with energy equal to or greater than its band gap, resulting in the excitation of electrons from the valence band (VB) to the conduction band (CB), leaving behind holes in the VB. The incorporation of Nd^{3+} ions and the conductive GO matrix facilitated the effective separation and migration of the photogenerated electron–hole pairs, thereby minimizing their recombination. The electrons were efficiently transferred to the GO sheets and further to adsorbed oxygen molecules, reducing them to superoxide radicals ($\cdot O_2^-$), while the photogenerated holes reacted with the surface-adsorbed water or hydroxide ions to generate hydroxyl radicals (·OH). The hole pairs occupied by GO nanosheets and the conduction band of the Nd@ZnS formed oxygen-based superoxide radicals ($O_2^{\bullet-}$) (eqn (1.5)). Upon protonation, the $O_2^{\bullet-}$ radicals produced the hydroxyl radicals ($HO_2^{\bullet-}$) that caused the generation of hydroxyl radicals from CODs using Nd@ZnS: GO-NSs (Fig. 5c).

$$\text{Nd@ZnS:GO-NSs} + h\nu \rightarrow \text{Nd@ZnS}\,(h^+) + \text{2D-GO nanosheet}\,(e^-) \quad (1.4)$$

$$O_2 + \text{2D-GO nanosheet}\,(e^-) \rightarrow + O_2^{\bullet -} \quad (1.5)$$

$$OH_2 + \text{Nd@ZnS}\,(h^+) \rightarrow {}^{\bullet}OH, \quad (1.6)$$

$$O_2^{\bullet -} + H_2O \rightarrow HO_2^{\bullet} + OH^- \quad (1.7)$$

$$\text{2D-GO nanosheet}\,(e^-) + HO_2^{\bullet} + H^+ \rightarrow H_2O_2 \quad (1.8)$$

$$\text{2D-GO nanosheet}\,(e^-) + H_2O_2 \rightarrow {}^{\bullet}OH + OH^- \quad (1.9)$$

$$OH^- + \text{Nd@ZnS}\,(h^+) \rightarrow \text{Nd@ZnS} + {}^{\bullet}OH \quad (1.10)$$

These reactive oxygen species (ROS) exhibited strong oxidative potential and were primarily responsible for the breakdown of dye molecules.[39] The degradation occurred through the attack on the chromophoric centers of the dye, resulting in the cleavage of conjugated bonds and the formation of less toxic, colourless intermediate products or mineralized end products such as CO_2 and H_2O. As the dye molecules decomposed, their fragments desorbed from the catalyst surface, effectively regenerating the active sites of Nd@ZnS:GO-NSs for successive catalytic cycles.

Conclusion

In summary, this study reports a simple and effective neodymium-doped zinc sulfide (ZnS)-anchored graphene oxide (GO) nanosphere (Nd@ZnS:GO-NS) composite *via* co-precipitation and sonochemical techniques, followed by a surface charge-induced strained wrapping phenomenon. The Nd@ZnS:GO-NSs were formed by rolling up annealed GO nanosheets on Nd@ZnS nanoparticles, with diameters ranging ~150 nm. The final structure consisted of Nd@ZnS nanoparticles wrapped in GO nanosheets. Nd@ZnS and Nd@ZnS:GO-NSs were employed as photocatalysts for the degradation of CODs, MO and Coomassie BBR, in particular. Optimal photodegradation conditions were determined to be pH 8, COD dosage of 20 mgL^{-1}, and a Nd@ZnS:GO-NSs dosage of 20 mg, which resulted in excellent degradation efficiency. This work corroborated that both Nd@ZnS and Nd@ZnS:GO-NSs functioned as photocatalysts. However, Nd@ZnS:GO-NSs exhibited higher photodegradation efficiency, highlighting the supplementary role of the GO nanosheet. Additionally, Nd@ZnS:GO-NSs demonstrated reusability for up to six cycles. The hole pairs generated by Nd@ZnS:GO-NSs interacted more effectively with MO dye (with the azo (–N═N–) and single SO_3^- groups) than with BBR (which contained two SO_3^- groups and a quaternary nitrogen (═N^+) group). Thus, Nd@ZnS:GO-NSs present new opportunities for both fundamental research and practical applications. Furthermore, their properties can be enhanced by doping with other nanomaterials and fabricating related nanostructures.

Data availability

The data supporting this article have been included as part of the ESI† file, which is easily available on the journal websites.

Conflicts of interest

The author confirms that there is no conflict of interest.

Acknowledgements

There was no funding source. The author is thankful to the Central University of Gujarat and CSIR-CSMCRI, Bhavnagar, Gujarat, India, for providing the infrastructure and instrumental facilities.

References

1 J. Singh, S. Kumar, Rishikesh, A. K. Manna and R. K. Soni, *Opt. Mater.*, 2020, **107**, 110138.
2 T. A. Saleh, *Environ. Technol. Innovation*, 2021, **24**, 101821.
3 Z. H. Yang, J. Cao, Y. P. Chen, X. Li, W. P. Xiong, Y. Y. Zhou, C. Y. Zhou, R. Xu and Y. R. Zhang, *Microporous Mesoporous Mater.*, 2019, **277**, 277–285.
4 Y. Li, Z. Yin, G. Ji, Z. Liang, Y. Xue and Y. Guo, *Appl. Catal., B*, 2019, **246**, 12.
5 M. Sun, J. Ma, M. Zhang, Y. Xiao, Y. Zhu and S. Zhang, *Mater. Chem. Phys.*, 2020, **241**, 122450.
6 R. Gang, L. Xu, Y. Xia, J. Cai, L. Zhang, S. Wang and R. Li, *J. Colloid Interface Sci.*, 2020, **579**, 853–861.
7 R. Jain, M. Mathur, S. Sikarwar and A. Mittal, *J. Environ. Manage.*, 2007, **85**, 956–964.
8 Y. Shi, H. Wang, G. Song, Y. Zhang, L. Tong, Y. Sun and G. Ding, *RSC Adv.*, 2022, 21026–21040.
9 C. H. Han, H. D. Park, S. B. Kim, V. Yargeau, J. W. Choi, S. H. Lee and J. A. Park, *Water Res.*, 2020, **172**, 115514.
10 D. D. Dietz, K. M. Abdo, S. L. Eustis and J. E. Huff, *Toxicol. Sci.*, 1991, **17**, 335–346.
11 R. Gade, J. Ahemed, K. L. Yanapu, S. Y. Abate, Y. T. Tao and S. Pola, *J. Environ. Chem. Eng.*, 2018, **6**, 4504–4513.
12 S. Fentie Tadesse, D. H. Kuo, W. Lakew Kebede and G. S. Wolde, *Appl. Surf. Sci.*, 2021, **569**, 151091.
13 J. Dadashi, M. A. Ghasemzadeh and M. Salavati-Niasari, *RSC Adv.*, 2022, **12**, 23481–23502.
14 H. Rashidi Nodeh, H. Sereshti, E. Beirakabadi and K. Razmkhah, *Int. J. Environ. Sci. Technol.*, 2020, **17**, 819–828.
15 S. K. Sahoo, S. Padhiari, S. K. Biswal, B. B. Panda and G. Hota, *Mater. Chem. Phys.*, 2020, **244**, 122710.
16 E. H. Hong, K. H. Lee, S. H. Oh and C. G. Park, *Adv. Funct. Mater.*, 2003, **13**, 961–966.
17 A. Gupta, J. Kaur and O. P. Pandey, *Phys. Status Solidi A*, 2023, **220**, 2300028.
18 H. Karimi, H. R. Rajabi and L. Kavoshi, *J. Photochem. Photobiol., A*, 2020, **397**, 112534.

19 C. H. Lai, M. Y. Lu and L. J. Chen, *J. Mater. Chem.*, 2012, **22**, 19–30.
20 I. Rašović, *Mater. Sci. Technol.*, 2016, **33**(7), 777–794.
21 R. Ramachandran, M. Saranya, P. Kollu, B. P. C. Raghupathy, S. K. Jeong and A. N. Grace, *Electrochim. Acta*, 2015, **178**, 647–657.
22 Y. Hanifehpour, B. Soltani, A. R. Amani-Ghadim, B. Hedayati, B. Khomami and S. W. Joo, *J. Ind. Eng. Chem.*, 2016, **34**, 41–50.
23 R. Saravanan, V. K. Gupta, V. Narayanan and A. Stephen, *J. Mol. Liq.*, 2013, **181**, 133–141.
24 Y. Qin, Z. Sun, W. Zhao, Z. Liu, D. Ni and Z. Ma, *Nano-Struct. Nano-Objects*, 2017, **10**, 176–181.
25 A. T. Smith, A. M. LaChance, S. Zeng, B. Liu and L. Sun, *Nano Mater. Sci.*, 2019, **1**, 31–47.
26 T. Moskalewicz, M. Warcaba, A. Łukaszczyk, M. Kot, A. Kopia, Z. Hadzhieva and A. R. Boccaccini, *Appl. Surf. Sci.*, 2022, **575**, 151688.
27 A. Phuruangrat, T. Thongtem and S. Thongtem, *Chalcogenide Lett.*, 2011, **8**, 291–295.
28 H. Wu, L. Li, K. Chang, K. Du, C. Shen, S. Zhou, G. Sheng, W. Linghu, T. Hayat and X. Guo, *J. Environ. Chem. Eng.*, 2020, **8**(4), 103882.
29 H. Qu, G. Su, W. Liu and C. Xia, *J. Nanopart. Res.*, 2014, **16**(12), 2762.
30 Z. Quan, Z. Wang, P. Yang, J. Lin and J. Fang, *Inorg. Chem.*, 2007, **46**(4), 1354–1360.
31 J. Zheng, H. Liu, B. Wu, Y. Guo, T. Wu, G. Yu, Y. Liu and D. Zhu, *Nano Res.*, 2011, **4**(7), 705–711.
32 D. Chen, D. Wang, Q. Ge, G. Ping, M. Fan, L. Qin, L. Bai, C. Lv and K. Shu, *Thin Solid Films*, 2015, **574**, 1–9.
33 P. Devendran, D. Selvakumar, G. Ramadoss, R. Sivaramakrishnan, T. Alagesan, R. Jayavel and K. Pandian, *Chemosphere*, 2022, **287**, 132091.
34 A. Deptula, M. Wade, S. A. Rogers and R. M. Espinosa-marzal, *Adv. Funct. Mater.*, 2022, 2111414, 1–14.
35 H. Karimi, H. Reza and L. Kavoshi, *J. Photochem. Photobiol., A*, 2020, **397**, 112534.
36 C. Wang, M. Chen, J. Wu, F. Mo and Y. Fu, *Anal. Chim. Acta*, 2019, **1086**, 66–74.
37 S. Haji, B. Benstaali and N. Al-bastaki, *Chem. Eng. J.*, 2011, **168**, 134–139.
38 B. Li, T. Liu, Y. Wang and Z. Wang, *J. Colloid Interface Sci.*, 2012, **377**, 114–121.
39 C.-L. Song, Z. Li, Y.-N. Zhang, G. Zhang and Y.-W. Yang, *Supramol. Mater.*, 2023, **2**, 100035.